



# Optimizing Interface Conductivity in Electronics



The latest eBook from  
**Advanced Optical Metrology.**  
Download for free.

Surface roughness is a key parameter for judging the performance of a given material's surface quality for its electronic application. A powerful tool to measure surface roughness is 3D laser scanning confocal microscopy (LSM), which will allow you to assess roughness and compare production and finishing methods, and improve these methods based on mathematical models.

Focus on creating high-conductivity electronic devices with minimal power loss using laser scanning microscopy is an effective tool to discern a variety of roughness parameters.

**EVIDENT**  
**OLYMPUS**

**WILEY**

# Excellent Long-Range Charge-Carrier Mobility in 2D Perovskites


Manuel Kober-Czerny, Silvia Genaro Motti, Philippe Holzhey, Bernard Wenger, Jongchul Lim,\* Laura Maria Herz,\* and Henry James Snaith\*

The use of layered, 2D perovskites can improve the stability of metal halide perovskite thin films and devices. However, the charge carrier transport properties in layered perovskites are still not fully understood. Here, the sum of the electron and hole mobilities ( $\Sigma\mu$ ) in thin films of the 2D perovskite  $\text{PEA}_2\text{PbI}_4$ , through transient electronically contacted nanosecond-to-millisecond photoconductivity measurements, which are sensitive to long-time, long-range (micrometer length scale) transport processes is investigated. After careful analysis, accounting for both early-time recombination and the evolution of the exciton-to-free-carrier population, a long-range mobility of  $8.0 \pm 0.6 \text{ cm}^2 (\text{V s})^{-1}$ , which is ten times greater than the long-range mobility of a comparable 3D material  $\text{FA}_{0.9}\text{Cs}_{0.1}\text{PbI}_3$  is determined. These values are compared to ultra-fast transient time-resolved THz photoconductivity measurements, which are sensitive to early-time, shorter-range (tens of nm length scale) mobilities. Mobilities of 8 and  $45 \text{ cm}^2 (\text{V s})^{-1}$  in the case of the  $\text{PEA}_2\text{PbI}_4$  and  $\text{FA}_{0.9}\text{Cs}_{0.1}\text{PbI}_3$ , respectively, are obtained. This previously unreported concurrence between the long-range and short-range mobility in a 2D material indicates that the polycrystalline thin films already have single-crystal-like qualities. Hence, their fundamental charge carrier transport properties should aid device performance.

## 1. Introduction

More than a decade after their first introduction as light absorbing materials in solar cells in 2009, metal halide perovskites continue to be at the forefront of photovoltaic (PV)

M. Kober-Czerny, S. G. Motti, P. Holzhey, B. Wenger, J. Lim,<sup>[†]</sup> L. M. Herz, H. J. Snaith  
Department of Physics  
University of Oxford  
Oxford OX1 2JD, UK  
E-mail: jclim@cnu.ac.kr; laura.herz@physics.ox.ac.uk;  
henry.snaith@physics.ox.ac.uk

 The ORCID identification number(s) for the author(s) of this article can be found under <https://doi.org/10.1002/adfm.202203064>.

© 2022 The Authors. Advanced Functional Materials published by Wiley-VCH GmbH. This is an open access article under the terms of the Creative Commons Attribution License, which permits use, distribution and reproduction in any medium, provided the original work is properly cited.

<sup>[†]</sup>Present address: Graduate school of Energy Science and Technology, Chungnam National University, Yuseong-gu, Daejeon, 34134, Republic of Korea

DOI: 10.1002/adfm.202203064

research.<sup>[1]</sup> After pioneering work demonstrating high efficiency in PV devices in 2012, the research has flourished around these materials with stoichiometry  $\text{AMX}_3$  (typically A = methylammonium ( $\text{MA}^+$ ), formamidinium ( $\text{FA}^+$ ), or cesium ( $\text{Cs}^+$ ); M = lead ( $\text{Pb}^{2+}$ ) or tin ( $\text{Sn}^{2+}$ ); X = iodide ( $\text{I}^-$ ), bromide ( $\text{Br}^-$ ), or chloride ( $\text{Cl}^-$ )).<sup>[2–5]</sup>

Beyond the 3D perovskites, 2D Ruddlesden–Popper (RP) and Dion–Jacobson (DJ) structures are considered to be possible alternatives to increase the stability of the perovskite layer and allowing for the bandgap and optical properties to be adjusted by varying the “quantum well” width and confinement.<sup>[6–10]</sup> The RP-phase has a stoichiometry of  $\text{A}'_2\text{A}_{n-1}\text{M}_n\text{X}_{3n+1}$ , where A' is now a larger organic ion (most commonly butylammonium ( $\text{BA}^+$ ) or phenylethylammonium ( $\text{PEA}^+$ )).<sup>[11]</sup> This organic ion induces the layered structure by separating  $n$ -stacks of  $[\text{MX}_6]^{4-}$  octahedra that are generally oriented parallel to an underlying substrate.<sup>[12]</sup> This directly affects the bandgap and band structure

and hence optoelectronic properties, such as photoluminescence energy and charge carrier transport.<sup>[13]</sup> The latter one is quantified by the charge carrier mobility ( $\mu$ ). Under the influence of an electric field, the mobility of a charge carrier in a solid-state lattice is represented by its reduced mass ( $m^*$ ), the elemental charge, and the mean time between scattering events with the lattice ( $\tau_{sc}$ )<sup>[14]</sup>

$$\mu = \frac{e \cdot \tau_{sc}}{m^*} \quad (1)$$

It is a crucial material quality, but it must be acquired carefully. For instance, for  $\text{MAPbI}_3$ , the archetypical metal halide perovskite composition, the reported mobility values span three orders of magnitude.<sup>[15]</sup> Some of these discrepancies are caused by real differences in the morphology of the material, for instance highly defective polycrystalline films versus improved-crystallinity thin films or single crystals.<sup>[16–19]</sup> Other variations arise from the length scales probed (few nm vs many microns or mm), and from inappropriate application of measurement techniques based on false assumptions.<sup>[15,20]</sup>  $\mu$  can be related to the conductivity of a material. Here, we use that relation to calculate the mobility from a conductivity signal acquired from transient

photoconductivity (TPC) or optical-pump terahertz-probe spectroscopy (OPTP)

$$\sigma_{t=0} = \mu \cdot N_0 \phi \cdot e \quad (2)$$

where  $\sigma_{t=0}$  is the conductivity signal extrapolated to  $t = 0$ ,  $\phi$  is the free carrier fraction in equilibrium, and  $N_0$  is the total number charge carriers per unit volume, which includes free charge carriers ( $N = N_0 \phi$ ) and coulombically bound charge carrier pairs (excitons). A good estimate of  $\phi$  is needed, to accurately calculate the mobility of a material. In case of the OPTP experiment, the time-scale probe is  $<1$  ns, short enough, so that no equilibrium of free carriers and excitons has formed yet and  $\phi$  can be approximated as 1. While the assumption of  $\phi = 1$  is also true for the 100 s of ns, long-range, TPC measurement of 3D perovskites, such as MAPbI<sub>3</sub> or FA<sub>0.9</sub>CS<sub>0.1</sub>PbI<sub>3</sub> at low charge carrier densities, it certainly is not true at higher charge carrier densities due to the law of mass action, as has been investigated in a recent study.<sup>[21]</sup>

2D RP perovskites with  $n < 5$  have exciton binding energies on the order of or greater than 100 meV and are considered to be “excitonic materials”, since a significant fraction of excitons is formed following photoexcitation.<sup>[22]</sup> Excitons, as pseudo particles with a net charge of zero, do not drift in an electric field and so do not contribute to conductivity. Therefore, the assumption  $\phi = 1$  is also not true for 2D perovskites, such as PEA<sub>2</sub>PbI<sub>4</sub>. It is worth emphasizing the importance of precise reporting of the mobility investigated at this point: There is a risk of presenting confusing, even contradictory results when studying excitons and mobile carriers, using long-range and short-range measurement techniques. This is even more true for 2D perovskites, having an in-plane and out-of-plane anisotropy of properties.

The “out-of-plane” charge carrier transport and mobility of 2D perovskites are generally accepted to be much lower than the “in-plane” mobility (here out-/in-plane correspond to the crystallographic planes due to the anisotropy of the 2D system) and great effort has been put into understanding and improving it.<sup>[23,24]</sup> This anisotropy can lead to reduced PV device performance, when charge carriers have to move across the crystallographic planes of the 2D perovskites.<sup>[25]</sup>

Indeed, the stability-enhancement by the 2D perovskite phases is often thought to come at the expense of carrier conductivity and mobility.<sup>[23,26,27]</sup> Early research on layered tin-halide perovskites, however, theorized that decreased conductivity could be accompanied by an increase in mobility—that is free charge carrier mobility in the 2D plane.<sup>[28]</sup>

For vertical device architectures, advances in film fabrication have resulted in improved control over layer orientation and, in some cases, full conversion into vertically oriented 2D layers, enabling transport along the 2D perovskite sheets, in a direction normal to the substrate.<sup>[8,29–31]</sup>

To better understand the underlying physics of the charge carrier transport in 2D perovskites, we study PEA<sub>2</sub>PbI<sub>4</sub> ( $n = 1$ ) as a model 2D system, since it is one of the most researched layered perovskites and hence allows for best comparison of our results. Additionally, solution-processed  $n = 1$  thin films do not face the same phase impurity challenges as observed for  $n > 1$  2D perovskites and are generally more oriented.<sup>[12,32–38]</sup>

PEA<sub>2</sub>PbI<sub>4</sub> is described in early reports as a dielectrically confined system with exciton binding energies of  $\approx 230$  meV.<sup>[39]</sup> A recent diffusivity study of PEA<sub>2</sub>PbI<sub>4</sub> has observed highly mobile excitonic species.<sup>[40]</sup> Simultaneously, free carrier behavior has been observed and is being investigated. In a recent report, a polaron model is proposed to explain free carrier transport in PEA<sub>2</sub>PbI<sub>4</sub>.<sup>[41]</sup>

In this study, we focus on investigating the in-plane mobility and photophysical properties, by measuring the lateral long-range and short-range conductivity of highly oriented thin films. We gain a better understanding of the generation and transport properties of free charge carriers in PEA<sub>2</sub>PbI<sub>4</sub> over both length scales. This allows us to postulate possible ways to make 2D perovskites in general more useful in optoelectronic device applications. In this work, we use the word “free carrier,” but want to emphasize that the exact nature of carriers in a 2D perovskite is part of ongoing research. Whether it is true free carriers, polarons, or something else entirely should not affect the results obtained by our measurements, as any type of unpaired charge carrier will be probed and is hence part of the result.

## 2. Results

### 2.1. Structural Properties of 2D and 3D Perovskite Thin Films

As a first step in our investigation, we analyze the structure and morphology of the PEA<sub>2</sub>PbI<sub>4</sub> thin films. For this study, it is important to have a pure 2D perovskite phase with nearly perfectly oriented layers, in order to reduce the effects of multiple phases or anisotropy on the measured conductivity. Our optimized, simple fabrication method (see the Experimental Section) yielded highly oriented, large grains. We show scanning electron microscope (SEM) top images of a PEA<sub>2</sub>PbI<sub>4</sub> thin film, and compare these to those for a typical 3D perovskite FA<sub>0.9</sub>CS<sub>0.1</sub>PbI<sub>3</sub> in Figure 1A,B. There are strikingly large grain sizes (as resolved in the SEM images) for 2D perovskite films. We note that although the 3D perovskite films appear in the SEM image as much rougher on the 100’s nm length scale with much smaller polycrystalline grain size than the 2D perovskite films, both types of films appear extremely smooth and specular (shiny) on the optical length scale. Grain sizes in the tens to hundreds of nm length scales are also typical for 3D perovskite films processed from mixed solvent systems via the antisolvent quenching method that we have employed here.<sup>[42]</sup> We also note that even after careful optimization, we were not able to significantly enhance the grain size in the 3D perovskite films, but this is representative of a typical 3D perovskite thin film. In Figure 1C,D, we compare 2D X-ray diffraction (XRD) scans for similar films: For the 3D perovskite films, the XRD peaks appear as semicircles in the  $q_{xy}$   $q_z$  plot, indicative of a low degree of texturing and a random distribution of crystalline orientations. In contrast, the majority of the scattering intensity is in the  $q_{xy} = 0$  direction for the 2D perovskite film, consistent with highly textured orientated films, with the perovskite 2D planes lying parallel to the substrate.<sup>[12,43]</sup> Figure 1E,F shows the difference between the 3D and 2D perovskite thin films schematically. We also present the 1D XRD for PEA<sub>2</sub>PbI<sub>4</sub> and FA<sub>0.9</sub>CS<sub>0.1</sub>PbI<sub>3</sub> in Figure S1 in the Supporting Information. It is

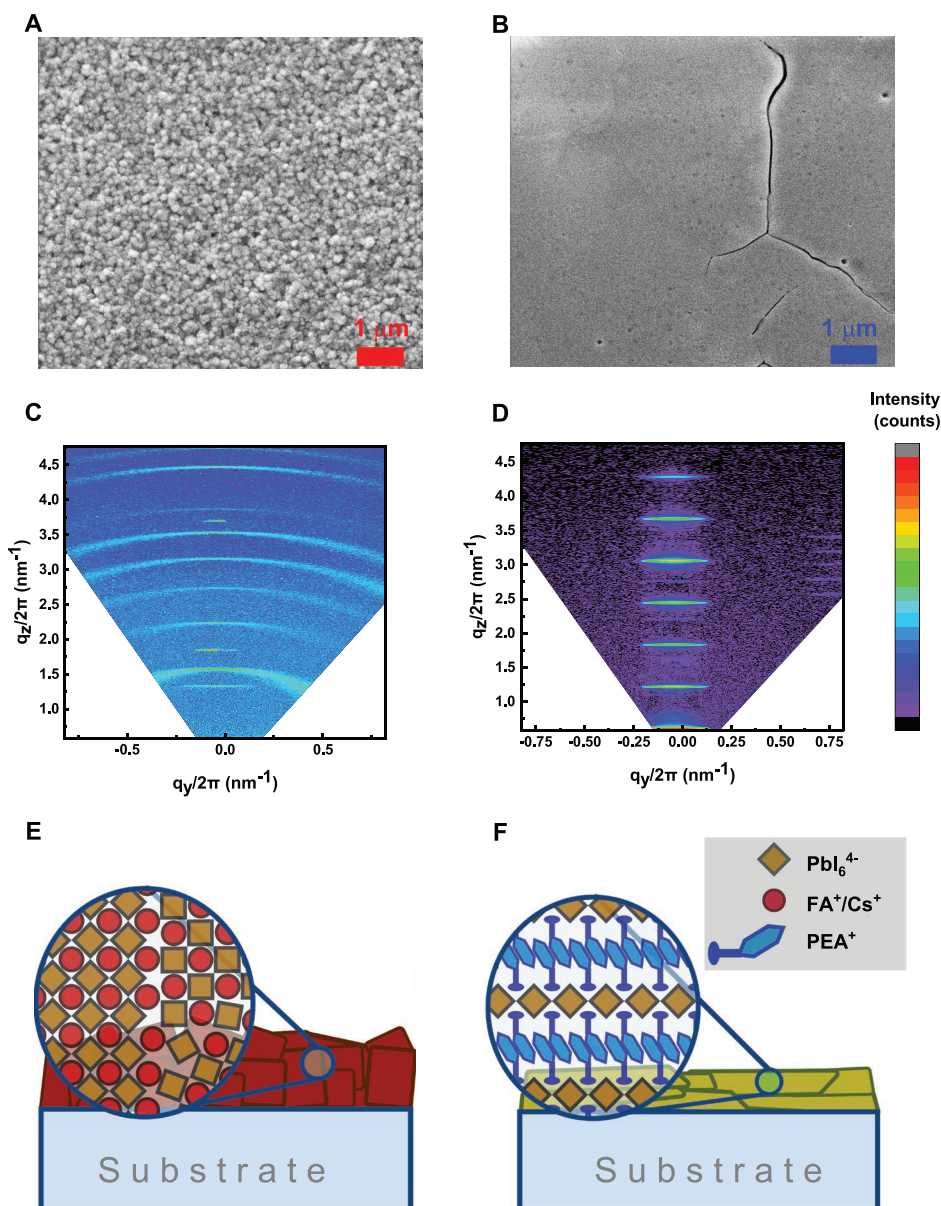


**Figure 1.** A/B) 2D XRD scans of A)  $\text{FA}_{0.9}\text{Cs}_{0.1}\text{PbI}_3$  and B)  $\text{PEA}_2\text{PbI}_4$ . C/D) Top view SEM images for C)  $\text{FA}_{0.9}\text{Cs}_{0.1}\text{PbI}_3$  and D)  $\text{PEA}_2\text{PbI}_4$ . E/F) Schematics showing the structure of a E) 3D and F) 2D  $n=1$  perovskite, which may explain the more ordered nature of the polycrystalline thin film of the 2D material.

worth mentioning that the results presented in this work may be impacted by the reduced number of grain boundaries, an increased crystallinity as well as a combination of both and it is part of ongoing research to disentangle these effects.<sup>[44–46]</sup>

Next, we will investigate the “long-range” mobility of charge carriers in  $\text{PEA}_2\text{PbI}_4$  and  $\text{FA}_{0.9}\text{Cs}_{0.1}\text{PbI}_3$  thin films employing TPC.<sup>[21]</sup>

## 2.2. Understanding Exciton and Free Carrier Dynamics

In the TPC experiment, transistor-type electrode-gap devices, which probe the transport in a direction parallel to the plane of the substrate, are illuminated with a short (ns) above band

gap laser pulse, and the transient conductivity is recorded.<sup>[21]</sup> We give full details in the Supporting Information, but briefly, during and following the photoexcitation pulse, free carriers are generated which result in the photoconductivity signal. In 3D bulk perovskites, where exciton binding energies are low, we often expect that all of the absorbed photons lead to the generation of free carriers. However, the population is reduced in comparison to this maximum possible population, by two main contributions: an early-time recombination of generated carriers within the time-frame of the photo-excitation pulse, and an equilibrium between the free carrier and exciton populations, with the latter depending upon both charge-carrier density and exciton binding energy ( $E_B$ ). In order to determine the mobility from the TPC decay, we need to be able to estimate the

corresponding free carrier density as a function of time, during the measurement. This is feasible if we have knowledge of all the parameters which govern charge recombination and the exciton-to-free-carrier branching ratio as a function of charge-carrier density for these materials.

In equilibrium, the rate of exciton dissociation into free carriers is balanced by the rate of exciton formation from free charge carriers, where the term free carriers refers to unbound electrons and holes present in the conduction and valance bands, respectively. This equilibrium can be calculated for each carrier concentration ( $N$ ) with knowledge of  $E_B$  using the Saha equation

$$N \cdot \frac{\phi^2}{1-\phi} = \left( \frac{2\pi \cdot \mu_0 \cdot k_B T}{h^2} \right)^{3/2} \cdot e^{-\frac{E_B}{k_B T}} \quad (3)$$

where  $\mu_0$  is the reduced carrier mass,  $k_B$  is the Boltzmann constant,  $T$  is the temperature, and  $h$  is the Planck's constant.<sup>[47]</sup> We note that this Saha equation is valid for our 2D perovskite assuming a quantum well thickness of  $\approx 15$  nm (see Section S8, Supporting Information for details).<sup>[41]</sup> The excitation used during the TPC experiment has a pulse width of  $\approx 3.7$  ns, which is much longer than typically observed carrier cooling phenomena.<sup>[48,49]</sup> Hence, we assume a pseudo-equilibrium of free carriers and excitons to have formed after the pulse, which can then be approximated by Equation (3).

The exciton binding energy of a material at room temperature can be estimated from its absorption coefficient ( $\alpha$ ). In Figure 2A, we show  $\alpha$  as obtained from transmittance and reflectance measurements for  $\text{FA}_{0.9}\text{Cs}_{0.1}\text{PbI}_3$  and  $\text{PEA}_2\text{PbI}_4$ . The latter is shifted toward higher energies and exhibit a strong characteristic peak near the absorption onset associated with

exciton formation.<sup>[11,40,50]</sup> Both absorption spectra can then be fitted individually with the ‘‘Elliott model’’ (see Section S3, Supporting Information for the details) to estimate  $E_B$  as well as the electronic bandgap of the continuum of states of each material (distinct from optical or Tauc estimates of the absorption onset energy).<sup>[51]</sup> From this, we find exciton binding energies of  $\approx 7$  meV (lit.: 5.3 meV) for the  $\text{FA}_{0.9}\text{Cs}_{0.1}\text{PbI}_3$  (bandgap of 1.55 eV, lit.: 1.51–1.57 eV) and  $\approx 230$  meV (lit.: 193–230 meV) for  $\text{PEA}_2\text{PbI}_4$  (bandgap of 2.63 eV, lit.: 2.36–2.63 eV).<sup>[43,52–56]</sup>

We can now apply the Saha equation (Equation (3)) to estimate the fraction of free carriers ( $\phi$ ) with respect to the total density of photoexcited species. The results are plotted in Figure 2B for materials with exciton binding energies of 7 and 230 meV, which reveals a significant reduction in the free carrier fraction in the latter case, in the range of carrier densities  $N$  that are typically associated with optoelectronic characterization methods ( $10^{13}$ – $10^{18}$   $\text{cm}^{-3}$ ). An assumption of  $\phi = 1$  for  $\text{FA}_{0.9}\text{Cs}_{0.1}\text{PbI}_3$  is valid for  $N < 10^{16}$   $\text{cm}^{-3}$  and corrections only need to be made for higher  $N$ , as has been described in previous work.<sup>[21]</sup>

In addition to modulating the fraction of free carriers, the high  $E_B$  will also affect the photoluminescence (PL) emission properties and charge carrier recombination occurring in the 2D material. The recombination of carriers can be assessed via time-resolved photoluminescence (TRPL) and photoluminescence quantum efficiency (PLQE) measurements. Following photo-excitation, the dynamics of charge carriers can be described by

$$\frac{dn}{dt} = G - k_1 n - k_{2,\text{eff}} n^2 - k_3 n^3; k_{2,\text{eff}} = \left( k_2 + \frac{k_{\text{ex}}}{n_{\text{eq}}} \right) \quad (4)$$

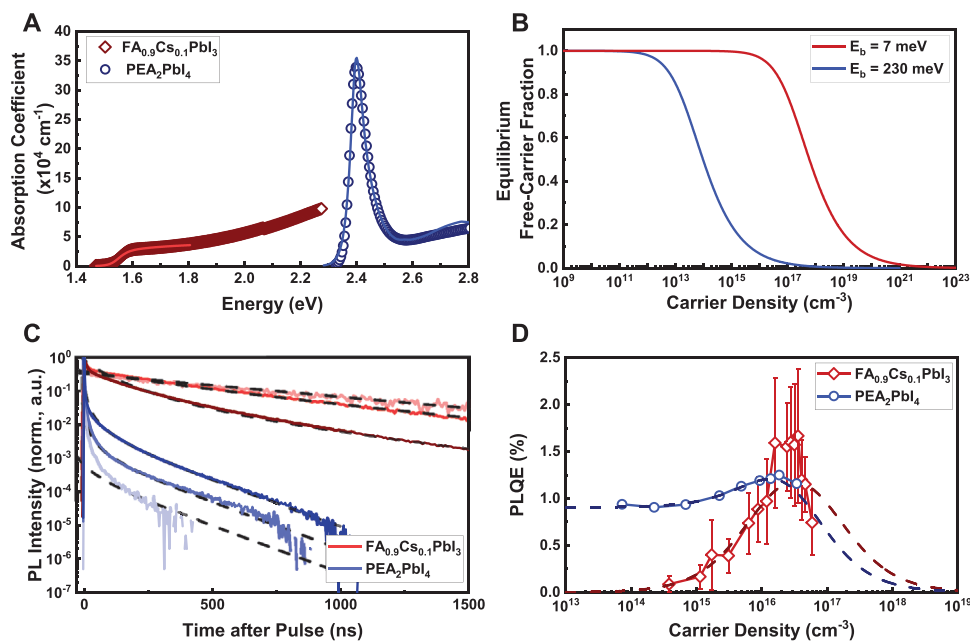


**Figure 2.** A) Absorption coefficients of both materials. The best Elliott fits (solid lines) are shown in both cases together with the resulting  $E_B$  of 7 and 230 meV for  $\text{FA}_{0.9}\text{Cs}_{0.1}\text{PbI}_3$  and  $\text{PEA}_2\text{PbI}_4$ , respectively. B) The free carrier fraction at room temperature for both calculated exciton binding energies as estimated from the Saha equation. C) Normalized time-resolved PL decays for both materials as measured for different excitation fluences (darkness of color; 2.2–220  $\text{nJ cm}^{-2}$ ). The background before the pulse has been subtracted. Dashed lines indicate global fits used for the two materials separately (details in Section S4, Supporting Information). D) Intensity-dependent PLQE measurements with corresponding error bars are shown (standard error from four films per material, three measured spots per sample). Fits to Equation (4) are presented as dashed lines.

**Table 1.** Recombination constants as obtained from both TRPL/PLQE fitting and OPTP spectroscopy. All values are compared to literature values.

Material	Method	$k_1$ [ $10^6 \text{ s}^{-1}$ ]	$k_{\text{ex}}$ [ $10^6 \text{ s}^{-1}$ ]	$k_2$ [ $10^{-10} \text{ cm}^3 \text{ s}^{-1}$ ]	$k_3$ [ $10^{-28} \text{ cm}^6 \text{ s}^{-1}$ ]
FA <sub>0.9</sub> Cs <sub>0.1</sub> PbI <sub>3</sub>	TRPL, PLQE	1.1	NA	0.9	7.2
	OPTP	–	NA	3.1	0.7
	Literature <sup>[57,58]</sup>	0.5-7	NA	1.1	0.2
PEA <sub>2</sub> PbI <sub>4</sub>	TRPL, PLQE	6.3	65	9.8	180
	OPTP	5.0	–	900	3.1
	Literature <sup>[23,37]</sup>	0.9	50	20	10–200

where  $G$  is the carrier generation rate,  $k_1$  and  $k_3$  are the rate constants for the nonradiative trap-assisted recombination and Auger recombination, respectively,  $k_2$  and  $k_{\text{ex}}$  are the rate constants for the radiative bimolecular (band-to-band) and exciton recombination, and  $n_{\text{eq}}$  is the free carrier density in equilibrium and equal to the either side of Equation (3) (see Section S4, Supporting Information for details).<sup>[41]</sup> In Figure 2C, we show the time-resolved PL decays for both, the 3D FA<sub>0.9</sub>Cs<sub>0.1</sub>PbI<sub>3</sub> and the 2D PEA<sub>2</sub>PbI<sub>4</sub> for a range of pulsed excitation fluences (notably the TCSPC pulse width is tens of ps, rather than ns for the TPC measurement). A stark difference in lifetimes between the 2D and 3D perovskites can be observed immediately: The 3D material shows a long PL decay of a few hundred nanoseconds, which is mostly happening in the monomolecular, trap-assisted regime as seen in Figure S4 in the Supporting Information. In contrast, the PL intensity of the 2D material drops by an order of magnitude within a few tens of nanoseconds, however, it still shows a significant PL signal after more than 200 ns, indicating the presence of longer-lived species. In a pulsed TRPL experiment, we can assume  $G = 0$  and  $k_3$  can be neglected at the fluences probed. Hence, the decay is dominated by trap-assisted recombination at later times. We globally fit these data using Equation (4), to extract a trap-assisted recombination constant  $k_1$  as well as  $k_{2,\text{eff}}$ . In Figure 2C, we show the resulting fits overlaid with the data for the full-time range. For FA<sub>0.9</sub>Cs<sub>0.1</sub>PbI<sub>3</sub>, we determine that  $k_1$  is  $7.5 \times 10^5 \text{ s}^{-1}$ , while it increases to  $6.3 \times 10^6 \text{ s}^{-1}$  for PEA<sub>2</sub>PbI<sub>4</sub> (see Supporting Information for more details).

To determine the higher-order recombination constants, we measured and assessed the fluence-dependent steady-state PLQE for these thin films (Figure 2D). Under continuous illumination, the PLQE of a material can be estimated as<sup>[37]</sup>

$$\text{PLQE} = \frac{k_{\text{ex}} + k_2 n}{k_{\text{ex}} + k_1 + k_2 n + k_3 n^2} \quad (5)$$

We note that for both, Equations (4) and (5), the quasi-first-order, radiative recombination of excitons ( $k_{\text{ex}}$ ) is usually neglected in 3D perovskites at room temperature, because of the low  $E_{\text{B}}$  in 3D lead halide perovskites and hence large value of  $\phi$  (see Section S4, Supporting Information for details).

Under continuous wave illumination, Equation (5) can then be used to estimate  $k_2$  and  $k_3$  (as well as  $k_{\text{ex}}$ ) from PLQE data. For FA<sub>0.9</sub>Cs<sub>0.1</sub>PbI<sub>3</sub>, we observe a monotonically increasing

PLQE up to a carrier density of  $2 \times 10^{16} \text{ cm}^{-3}$ . By fixing  $k_1$  to that derived from the transient PL, we obtained the best fit to the PLQE with  $k_2 = 8.79 \times 10^{-11} \text{ cm}^3 \text{ s}^{-1}$  and  $k_3 = 7.22 \times 10^{-28} \text{ cm}^6 \text{ s}^{-1}$ . The data and fit are shown in Figure 2D. In contrast to the 3D case, the PEA<sub>2</sub>PbI<sub>4</sub> thin films have an almost constant PLQE of  $\approx 1\%$  at the lower fluence range, and only exhibit a slight increase in PLQE as the excitation fluence is increased. This is a result of the excitonic nature of the PL emission as described previously, where the monomolecular radiative recombination of excitons is insensitive to excitation fluence.<sup>[37,41]</sup> The best fit was obtained for  $k_2 = 9.8 \times 10^{-10} \text{ cm}^3 \text{ s}^{-1}$  and  $k_3 = 1.8 \times 10^{-26} \text{ cm}^6 \text{ s}^{-1}$  and a  $k_{\text{ex}}$  of  $6.5 \times 10^7 \text{ s}^{-1}$ . We note that the accuracy of  $k_{\text{ex}}$  is relatively high, assuming that our  $k_1$  of  $6.3 \times 10^6 \text{ s}^{-1}$  determined from the TRPL is accurate. The accuracy of  $k_2$  is also relatively high, since there is small, but highly relevant increase in PLQE over the excitation range studied, due to the increasing competitiveness of the radiative  $k_2$  process over the nonradiative  $k_1$  process, over the intensity range of measurement. However, the accuracy of  $k_3$  is low, since there is very little data at high enough excitations to properly observe the expected roll-off in PLQE (all the fitting procedures are detailed in Section S4, Supporting Information).<sup>[10,37]</sup>

We later determine the same recombination constants using optical-pump terahertz probe (OPTP) spectroscopy. The OPTP experiment can record the photoconductivity transients at higher charge-carrier densities and with femtosecond resolution, and thus allows for more accurate determination of the higher-order decay rates,  $k_2$  and  $k_3$ . In Table 1, we show that the values obtained by both methods are in good agreement with one another and with previously reported values. In Figure S6 in the Supporting Information, we show the impact of an error in the recombination constants on the resulting mobility of PEA<sub>2</sub>PbI<sub>4</sub>. We conclude that the recombination constants are determined with enough accuracy so that the resulting error is lower than the batch-to-batch variation of our data.

### 2.3. Long-Range Mobility Calculation

TPC can be used to estimate the “long-range,” conductivity and mobility in a direction parallel to the substrate. Since we have already determined that the crystallographic planes of the 2D perovskites are highly ordered parallel to the plane of the substrate, we expect the TPC to also probe mostly the conductivity and mobility in the plane of the 2D perovskite sheets. Charge carriers are generated following photoexcitation by a few-ns pulse width excitation (10 Hz) and start drifting under a small applied electric field of  $<0.01 \text{ V } \mu\text{m}^{-1}$ . Concerning the length scale over which the charge transport will occur during the measurement, this will depend upon the charge carrier mobility, the charge carrier lifetime, and the applied electric field. For instance, with a mobility of  $1 \text{ cm}^2 \text{ V}^{-1} \text{ s}^{-1}$  and a lifetime of 1000 ns, the charge carriers would drift 1000 nm in the applied electric field of  $0.01 \text{ V } \mu\text{m}^{-1}$ .

The obtained conductivity decays are shown in Figure 3A (see Section S5, Supporting Information for details) for both PEA<sub>2</sub>PbI<sub>4</sub> and FA<sub>0.9</sub>Cs<sub>0.1</sub>PbI<sub>3</sub>. For both materials, we observe long-lived photoconductivity traces, with mono-exponential decay lifetimes of a few hundred nanoseconds, and peak

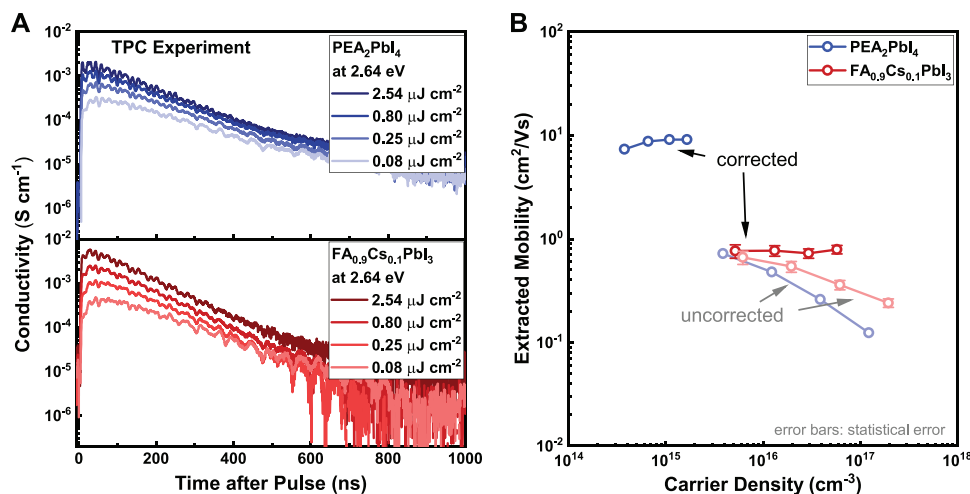


**Figure 3.** A) Transient photoconductivity decays after excitation by 2.64 eV (470 nm) pulsed laser with 10 Hz repetition rate for  $\text{PEA}_2\text{PbI}_4$  and  $\text{FA}_{0.9}\text{Cs}_{0.1}\text{PbI}_3$  at different excitation fluences (darkness of color; 0.08–2.54  $\mu\text{J cm}^{-2}$ ). B) The uncorrected  $\phi\Sigma\mu$  and corrected  $\Sigma\mu$  are shown for both materials with corresponding error bars (standard error from samples as described in Section S6, Supporting Information). In the first case, the carrier density is the excitation density, while in the latter case it is the estimated free carrier density. The two are shown in one plot to make the effect of the corrections as mentioned in Section S5 in the Supporting Information clearer.

conductivities between  $10^{-2}$  and  $10^{-4}$   $\text{S cm}^{-1}$ . If we were to follow the naïve approximations of neglecting early-time recombination during the photoexcitation pulse and assume that all absorbed photons lead to the generation of charge carriers at  $t = 0$ , Equation (1) would allow for an estimation of  $\phi\Sigma\mu$  when extrapolating the decays to extract the “ $t = 0$ ” conductivity at 0 ns, where  $\Sigma\mu$  is now the sum of both the electron and hole mobilities. The resulting  $\phi\Sigma\mu$  values determined in this manner are 0.1–0.7  $\text{cm}^2 (\text{V s})^{-1}$  in case of the  $\text{PEA}_2\text{PbI}_4$  and 0.2–0.7  $\text{cm}^2 (\text{V s})^{-1}$  for  $\text{FA}_{0.9}\text{Cs}_{0.1}\text{PbI}_3$ . The drop off in  $\phi\Sigma\mu$  determined in this manner with increasing excitation density is consistent with a reduction in  $\phi$  with increasing excitation density, and an increase in early-time recombination with increasing intensity. We note that over the range of excitation densities that we study here, we do not at any point observe a super-linear increase in peak photoconductivity with increasing excitation density. This implies that we are beyond the low charge density regime where trap filling may play a role.

The gained understanding of the early recombination processes as well as the behavior predicted by Equations (3) and (4) now allows us to correctly estimate  $\phi$  for both materials and to also account for early time recombination during the photoexcitation pulse. In practice, we simulate the charge-carrier density as a function of time during and following photoexcitation, using the parameters we have determined above and Equation (4). We then estimate the free carrier fraction for each time point using Saha’s equation (Equation (3)). The resulting time-dependent free carrier fraction will have a maximum value shortly after photoexcitation, which we use as our best estimate for  $\phi$ . We show the uncorrected  $\phi\Sigma\mu$  values side by side with the corrected  $\Sigma\mu$  values in Figure 3B. The fully corrected, accurate estimations of the mobilities are significantly different: in case of the 3D perovskite, the corrections affect the higher excitation densities more strongly with estimated free carrier fractions at peak conductivity (with respect to the initial excitation density) of 0.84, 0.68, 0.49, and 0.33, for excitation energies

of 0.08, 0.25, 0.80, and 2.54  $\text{nJ cm}^{-2}$ , respectively, with an average mobility of  $0.8 \pm 0.1 \text{ cm}^2 (\text{V s})^{-1}$  (average of three samples from one batch, and across all excitation energies). Other reports have estimated the long-range mobility of 3D perovskites as 0.2–6.7  $\text{cm}^2 (\text{V s})^{-1}$  (spread due to different preparation routes), using microwave conductivity, photo-induced transmission and reflection spectroscopy, or PL quenching.<sup>[15,21,58,59]</sup>

For  $\text{PEA}_2\text{PbI}_4$ , the free carrier fractions near peak conductivity are only 0.11, 0.07, 0.04, and 0.03, for the same range of excitation energies, resulting in  $\Sigma\mu$  of  $8.0 \pm 0.6 \text{ cm}^2 (\text{V s})^{-1}$  (average of 18 samples from six batches and across all excitation energies). We present both corrected and uncorrected (naïve approximations) mobilities side-by-side in Figure 3B, where the uncorrected  $\phi\Sigma\mu$  values are plotted against the excitation density, while the fully corrected  $\Sigma\mu$  are plotted against the peak carrier density. In both cases, the smaller relative errors of the estimated mobilities are consistent with the expectation that the mobility is widely independent of charge carrier densities in the regime measured here. It is worth emphasizing here that the low values of  $\phi$  in case of the 2D material can be mainly accounted for by the correction for the Saha equilibrium at a high exciton binding energy of 230 meV.

We note that for every trace, the carrier density, free-carrier-to-exciton-ratio, and fraction of bimolecular, excitonic, and monomolecular nonradiative recombination are all changing as a function of time, which are accounted for in a transient manner via our simulation and fitting protocol (see Section S5, Supporting Information).

#### 2.4. Short-Range Mobility Estimation

To further investigate both the early-time recombination processes, and to probe the early time “short-range” charge-carrier mobility, we have performed OPTP spectroscopy. For this technique, no electronic contact is made to the samples,

and the transient photoconductivity of the material, following photoexcitation, is determined by measuring the change in transmission of a THz-frequency probe beam. Similarly to the TPC measurement, the length scale over which OPTP spectroscopy probes the charge carrier mobility is dependent upon the absolute value of the charge carrier mobility. It is not straightforward to precisely estimate this length scale.<sup>[60]</sup> However, for metal halide perovskites it has been observed that the OPTP-estimated charge carrier mobility reduces when reducing perovskite nanocrystal sizes from 9 to 5 nm, suggesting that the length scale probe is on the order of 10 nm. Hence, we consider this short-range, in comparison to the length scale of 100 to 1000 s of nm probed by the TPC measurement. We show the transient OPTP photoconductivity decays in Figure 4A, again for both the 2D and 3D perovskite. We can observe that the OPTP transients of PEA<sub>2</sub>PbI<sub>4</sub> performed with 3.10 eV (400 nm) photoexcitation show a very fast decay component, within the first few picoseconds, which is not present

in the 3D sample. Since this early time decay for the transient OPTP signal in the PEA<sub>2</sub>PbI<sub>4</sub> samples is independent of excitation fluence, we cannot ascribe it to bimolecular or Auger recombination. Similar to earlier studies, we therefore interpret that this is due to the rapid exciton formation from an initial free carrier population, which are generated with photoexcitation energy significantly above the band gap, which relax to the conduction band edge and then into excitonic states, which are no longer sensed by the THz probe beam.<sup>[61,62]</sup> We further confirm this interpretation by photoexciting the same sample with a photon energy chosen to be resonant with the excitonic states (2.38 eV, 520 nm). We show these results in Figure 4B.

Consistently, when we excite the excitonic states directly, we no longer observe the early time drop in photoconductivity. Owing to the enhanced temporal resolution of the OPTP experiment, we are thus capable of measuring mobilities before exciton formation takes place and hence  $\phi$  is assumed to be close to 1 for the peak of the conductivity, since again, the

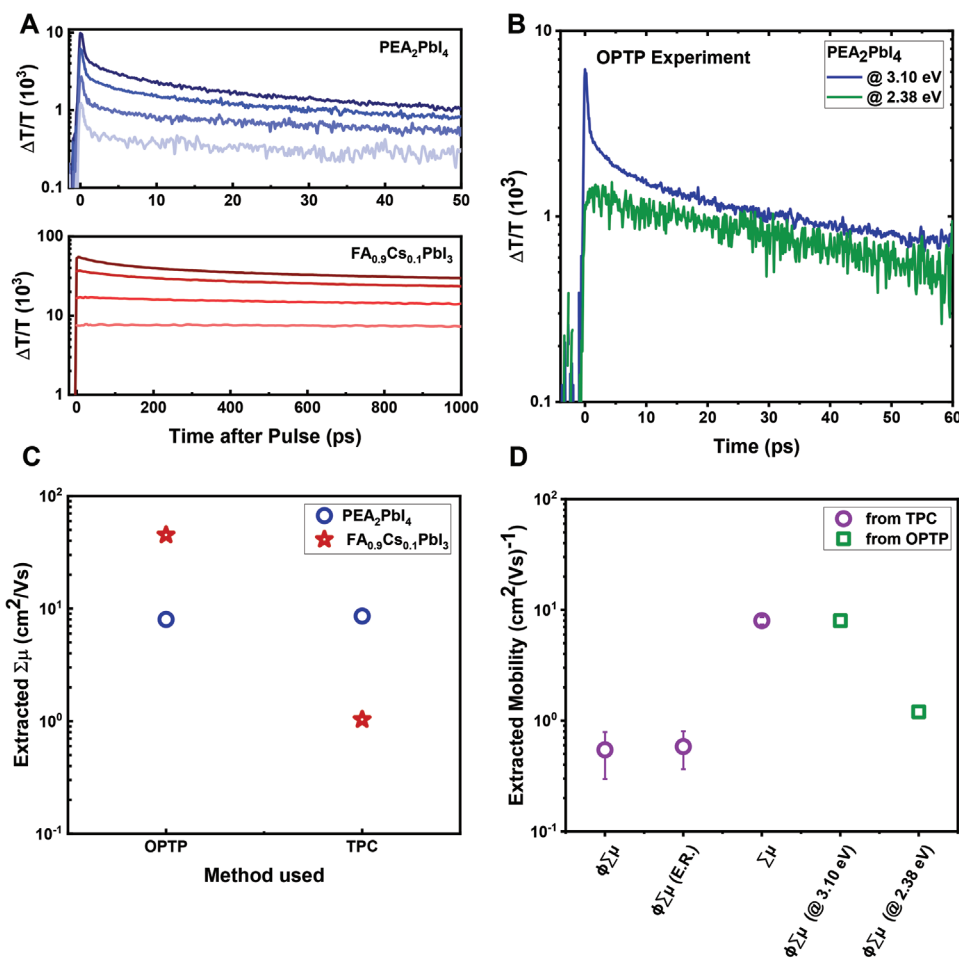


**Figure 4.** A) Terahertz conductivity decays extracted from the OPTP measurements of both materials pumped at 3.10 eV (400 nm) and different excitation fluences (darkness of color; 4.2–41.3  $\mu\text{J cm}^{-2}$ ). B) Terahertz conductivity decays extracted from the OPTP measurements of the PEA<sub>2</sub>PbI<sub>4</sub> thin films pumped at 3.10 eV (400 nm, continuum of states) and 2.38 eV (520 nm, exciton resonance). Both were measured at similar excitation fluences of 41.3  $\mu\text{J cm}^{-2}$ . C) Comparison of the extracted mobility of the two different methods used in this study. They represent short-range (OPTP) and long-range (TPC) measurements. D) Comparison of extracted mobilities for PEA<sub>2</sub>PbI<sub>4</sub> from all the different methods used in this study ( $\phi\Sigma\mu$  (E.R.) includes early-time recombination corrections, but not the Saha equation) with corresponding error bars (standard error from samples as described in Section S6, Supporting Information). It highlights the impact of an accurate estimation of free carriers on the resulting mobility.



photoexcitation photon energy (3.10 eV) directly excites carriers from the valence band into the continuum of states in the conduction band. We determine the THz charge carrier mobility from the peak photoconductivity signals to be  $\Sigma\mu = 40 \text{ cm}^2 (\text{V s})^{-1}$  for  $\text{FA}_{0.9}\text{Cs}_{0.1}\text{PbI}_3$  and  $8 \text{ cm}^2 (\text{V s})^{-1}$  for  $\text{PEA}_2\text{PbI}_4$ . It is worth mentioning again that the mobility estimated from OPTP is a relatively short-range mobility, owing to the high frequency of the THz probe.<sup>[15,63]</sup>

## 2.5. Combining Long-Range and Short-Range Measurements

Comparing the longer-range mobility that we have determined from the TPC measurements to the short-range mobility determined from the OPTP spectroscopy can yield valuable insights into the thin-film quality, and device relevance of the different materials, where longer range transport is required. Both data sets are summarized in Figure 4C. For the 3D perovskite  $\text{FA}_{0.9}\text{Cs}_{0.1}\text{PbI}_3$ , the short-range and long-range mobility differ by a factor of 50, a commonly known drop in similar materials.<sup>[15,58]</sup> A detailed understanding of the mechanisms behind this observation is part of ongoing research, but it indicates that longer-range defects responsible for charge carrier scattering are present in these polycrystalline thin films.<sup>[44–46]</sup> Encouragingly, for the 2D  $\text{PEA}_2\text{PbI}_4$ , the long-range and short-range mobility are almost identical, indicating close to “single-crystal-like” charge transport in these polycrystalline thin films. This coincidence of the short-range THz and long-range TPC mobility is a first for metal halide perovskites.

Notably, the THz mobility determined for the case for which we have pumped directly into excitonic states ( $\phi\Sigma\mu$  at 2.38 eV) is reduced by  $\approx 5.5$ -fold, delivering a  $\phi\Sigma\mu$  of  $1.5 \text{ cm}^2 (\text{V s})^{-1}$ . This is much closer to the TPC mobility determined when we have not accounted for the exciton fraction initially generated ( $\phi\Sigma\mu$  or  $\phi\Sigma\mu_{\text{E,R}}$ ) as shown in Figure 4D. This is not a coincidence since a larger density of excitons is initially formed when the sample is photoexcited in resonance with the excitonic states. The initial free carrier fraction will thus be much closer to the equilibrium value of  $\phi$  as governed by Equation (3). Two previous studies on  $\text{PEA}_2\text{PbI}_4$  have concluded that the Saha equation (Equation (3)) appears to accurately describe the equilibrium population in this material, consistent with both the fraction of early-time decay in the THz photoconductivity traces, and the intensity-dependent longer time measurements (like TPC).<sup>[61,64]</sup> This self-consistency within our data and with literature gives us a high level of confidence that our analysis and interpretations are correct.

## 3. Conclusions

In conclusion, we have shown that  $\text{PEA}_2\text{PbI}_4$  as a 2D perovskite has a considerably higher long-range mobility than a typical 3D perovskite used in archetypical PV devices. Critically, in  $\text{PEA}_2\text{PbI}_4$  thin films, the sum of mobilities is the same as determined by the measurements sensitive to both short-range and long-range transport. In contrast, the difference between short- and long-range mobility for 3D perovskites is often greater than

a factor of ten, and in the example we showed here, a factor of 50. This indicates that in these thin films of the 2D perovskite, there are no extrinsic defects responsible for charge carrier scattering, beyond those inducing short-range scattering events in the crystalline lattice. Thus, we can consider the 2D perovskite thin films studied here to charge transport properties similar to those in single crystals. Typically, researchers consider that the benefits of 2D perovskites are that they can passivate the surface of 3D phases and induce stability enhancements, in comparison to the neat 3D perovskite films, but that they are disadvantageous due to their perceived lower charge carrier mobility, resulting from the presence of the larger “insulating” planes of organic cations. However, our results here indicate that employing 2D perovskites, or using 2D perovskites to direct the crystallization of 3D perovskites, may indeed be a method to enhance the charge transport in optoelectronic devices. We therefore ascribe the often-observed underperformance of perovskites PV cells employing 2D phases, as compared to 3D phases, to two factors; a) the larger exciton binding energy which for a material such as  $\text{PEA}_2\text{PbI}_4$  results in 90% exciton formation at room temperature under solar irradiance. This by itself does not imply that 2D materials can never be useful as solar absorber materials. However, efforts may be required to either study and enhance exciton diffusion and ionization at the charge extraction interfaces or minimize nonradiative recombination losses within the 2D perovskite thin films. The latter would enable photon recycling and extremely long charge-carrier lifetimes to preserve the internal charge and exciton populations, while free carrier transport can allow “out-flow” of charge from the solar cells, with continuous re-population by the equilibrium between free carriers and excitons. b) The second factor, which we believe to be of secondary importance, is related to the anisotropy for charge transport and a persistent poor understanding of the impact of anisotropic charge carrier transport properties on the resulting device performance. Although substantial results have been achieved in the past, it remains a challenge to fully control the orientation of the 2D planes in perovskite thin films.<sup>[65]</sup> Yet, increasing efforts in developing means to control the orientation of the 2D planes with respect to the substrate will open possibilities of benefiting from enhanced anisotropic transport in different optoelectronic device architectures, including PV devices, light-emitting diodes, and radiation detectors, with both vertical “sandwich” structures, and lateral rear-contact structures. Improving understanding of how to control and make use of large exciton populations in 2D perovskites like  $\text{PEA}_2\text{PbI}_4$ , how to effectively passivate and inhibit nonradiative recombination, and how to best incorporate them into devices and interface with charge extraction/injection materials needs to be the focus of further research.

## 4. Experimental Section

**Materials:** Lead(II) iodide ( $\text{PbI}_2$ , 99.999%, metal basis) was purchased from TCI chemicals. Cesium iodide ( $\text{CsI}$ , 99.99%) was purchased from Alfa-Aesar. Formamidinium iodide (FAI) was purchased from GreatCell Solar. Phenylethylammonium iodide (PEAI), dimethylformamide (DMF, anhydrous, 99.8%), dimethyl sulfoxide (DMSO, anhydrous, >99.9%), anisole (anhydrous, 99.7%), isopropyl alcohol (IPA), and

acetone were purchased from Sigma-Aldrich. All chemicals were used as purchased without further purification unless stated otherwise.

**Glass Substrate Preparation:** Microscope glass substrates were cut to size (or 1 cm round quartz substrates were used) and then cleaned in an ultrasonic bath using a series of solvents:

1) 3 vol% Decon90 detergent in deionized H<sub>2</sub>O for 10 min, 2) rinsing with deionized H<sub>2</sub>O, 3) acetone for 10 min and 4) IPA for 10 min. The substrates were subsequently blown dry with N<sub>2</sub> gas. Prior to use they were treated with UV-ozone for 15 min.

**FA<sub>0.9</sub>Cs<sub>0.1</sub>PbI<sub>3</sub> Thin-Film Fabrication:** PbI<sub>2</sub>, FAI, and CsI were mixed in a nitrogen-filled glovebox to yield the exact stoichiometry of FA<sub>0.9</sub>Cs<sub>0.1</sub>PbI<sub>3</sub>. The precursors were then mixed with DMF:DMSO (3:1) to yield a 1.0 M precursor solution. After mixing for at least 3 h in the glovebox, 250 μL of solution was spin-coated dynamically onto clean glass or quartz substrates using a standardized program of 1000 rpm for 10 s then 5000 rpm (2000 rpm acceleration) for 35 s. The precursor solution was dropped at 5–6 s after the start of the program. Then, 350 μL of anisole was dropped onto the spinning film 35 s after the start of the program. It took 1–2 s to drop the anisole. Subsequently, the films were annealed at 100 °C for 15 min. The Au-electrode was evaporated as soon as possible after the films had cooled down.

**PEA<sub>2</sub>PbI<sub>4</sub> Thin-Film Fabrication:** Stoichiometric amounts of PbI<sub>2</sub> and PEAI were mixed in a nitrogen-filled glovebox with DMF to yield a 0.6 M precursor solution. After at least 3 h of mixing, the solution was spin-coated in a drybox using an optimized protocol: The film was spun at 1000 rpm for 10 s. After 5 s, 250 μL of precursor solution was dropped onto the spinning film. The spin speed was then increased to 6000 rpm (2000 rpm acceleration) for an additional 40 s. No antisolvent was needed. The films were annealed on a hotplate at 100 °C for 15 min. Au-electrodes were evaporated on top afterward.

**TPC Devices Fabrication:** After spin-coating the perovskite, 90 nm of gold (Au) was evaporated using a nano36 evaporator (Kurt J. Lesker) at <math>4 \times 10^{-6}</math> torr over the course of 15 min.

**Optoelectronic Characterization:** See the Supporting Information for detailed descriptions.

## Supporting Information

Supporting Information is available from the Wiley Online Library or from the author.

## Acknowledgements

This work was part funded by EPSRC, UK under EP/S004947/1 and EP/V010840/1. Financial support by the DFG via SPP2196 Priority Program (CH 1672/3-1) is gratefully acknowledged. J.L. was partially supported by the National Research Foundation of Korea (NRF-2021M3H4A1A02057007). The research leading to these results had received funding from the European Union's Horizon 2020 research and innovation program under grant agreements no. 764787 of the MAESTRO project and no. 861985 of the PEROCUBE project.

## Conflict of Interest

H.J.S. is cofounder and CSO of Oxford PV Ltd, a company commercializing perovskite PV technology.

## Data Availability Statement

The data that support the findings of this study are available from the corresponding author upon reasonable request.

## Keywords

2D Ruddlesden–Popper perovskites, charge carrier transport, mobility, thin films

Received: March 17, 2022

Revised: April 26, 2022

Published online: June 26, 2022

- [1] A. Kojima, K. Teshima, Y. Shirai, T. Miyasaka, *J. Am. Chem. Soc.* **2009**, *131*, 6050.
- [2] S. Wu, Z. Li, M. Q. Li, Y. Diao, F. Lin, T. Liu, J. Zhang, P. Tieu, W. Gao, F. Qi, X. Pan, Z. Xu, Z. Zhu, A. K. Y. Jen, *Nat. Nanotechnol.* **2020**, *15*, 934.
- [3] NREL, NREL Efficiency Chart, <https://www.nrel.gov/pv/cell-efficiency.html> (accessed: November 2021).
- [4] M. M. Lee, J. Teuscher, T. Miyasaka, T. N. Murakami, H. J. Snaith, *Science* **2012**, *338*, 643.
- [5] H. S. Kim, C. R. Lee, J. H. Im, K. B. Lee, T. Moehl, A. Marchioro, S. J. Moon, R. Humphry-Baker, J. H. Yum, J. E. Moser, M. Grätzel, N. G. Park, *Sci. Rep.* **2012**, *2*, 591.
- [6] I. C. Smith, E. T. Hoke, D. Solis-Ibarra, M. D. McGehee, H. I. Karunadasa, *Angew. Chem., Int. Ed.* **2014**, *53*, 11232.
- [7] G. Grancini, C. Roldán-Carmona, I. Zimmermann, E. Mosconi, X. Lee, D. Martineau, S. Narbey, F. Oswald, F. D. Angelis, M. Graetzel, M. K. Nazeeruddin, *Nat. Commun.* **2017**, *8*, 15684.
- [8] Y. Yang, C. Liu, A. Mahata, M. Li, C. Roldán-Carmona, Y. Ding, Z. Arain, W. Xu, Y. Yang, P. A. Schouwink, A. Züttel, F. D. Angelis, S. Dai, M. K. Nazeeruddin, *Energy Environ. Sci.* **2020**, *13*, 3093.
- [9] A. Krishna, S. Gottis, M. K. Nazeeruddin, F. Sauvage, *Adv. Funct. Mater.* **2019**, *29*, 1806482.
- [10] L. R. V. Buizza, T. W. Crothers, Z. Wang, J. B. Patel, R. L. Milot, H. J. Snaith, M. B. Johnston, L. M. Herz, *Adv. Funct. Mater.* **2019**, *29*, 1902656.
- [11] H. Tsai, W. Nie, J. C. Blancon, C. C. Stoumpos, R. Asadpour, B. Harutyunyan, A. J. Neukirch, R. Verduzco, J. J. Crochet, S. Tretiak, L. Pedesseau, J. Even, M. A. Alam, G. Gupta, J. Lou, P. M. Ajayan, M. J. Bedzyk, M. G. Kanatzidis, A. D. Mohite, *Nature* **2016**, *536*, 312.
- [12] D. H. Cao, C. C. Stoumpos, O. K. Farha, J. T. Hupp, M. G. Kanatzidis, *J. Am. Chem. Soc.* **2015**, *137*, 7843.
- [13] C. Otero-Martínez, J. Ye, J. Sung, I. Pastoriza-Santos, J. Pérez-Juste, Z. Xia, A. Rao, R. L. Z. Hoye, L. Polavarapu, *Adv. Mater.* **2021**, *34*, 2107105.
- [14] H. Ibach, H. Lüth, *Solid-State Physics*, Springer-Verlag, New York **2009**.
- [15] L. M. Herz, *ACS Energy Lett.* **2017**, *2*, 1539.
- [16] C. Wehrenfennig, G. E. Eperon, M. B. Johnston, H. J. Snaith, L. M. Herz, *Adv. Mater.* **2014**, *26*, 1584.
- [17] R. L. Milot, G. E. Eperon, H. J. Snaith, M. B. Johnston, L. M. Herz, *Adv. Funct. Mater.* **2015**, *25*, 6218.
- [18] D. A. Valverde-Chávez, C. S. Ponseca, C. C. Stoumpos, A. Yartsev, M. G. Kanatzidis, V. Sundström, D. G. Cooke, *Energy Environ. Sci.* **2015**, *8*, 3700.
- [19] O. E. Semonin, G. A. Elbaz, D. B. Straus, T. D. Hull, D. W. Paley, A. M. V. D. Zande, J. C. Hone, I. Kymissis, C. R. Kagan, X. Roy, J. S. Owen, *J. Phys. Chem. Lett.* **2016**, *7*, 3510.
- [20] E. A. Duijnste, J. M. Ball, V. M. L. Corre, L. J. A. Koster, H. J. Snaith, J. Lim, *ACS Energy Lett.* **2020**, *5*, 376.
- [21] J. Lim, M. Kober-Czerny, Y.-H. Lin, J. M. Ball, N. Sakai, E. A. Duijnste, M. J. Hong, J. G. Labram, B. Wenger, H. J. Snaith, *Nat. Commun.* **2022**, (unpublished).
- [22] T. Ishihara, J. Takahashi, T. Goto, *Solid State Commun.* **1989**, *69*, 933.

- [23] R. L. Milot, R. J. Sutton, G. E. Eperon, A. A. Haghighirad, J. M. Hardigree, L. Miranda, H. J. Snaith, M. B. Johnston, L. M. Herz, *Nano Lett.* **2016**, *16*, 7001.
- [24] M. Yu, C. Yi, N. Wang, L. Zhang, R. Zou, Y. Tong, H. Chen, Y. Cao, Y. He, Y. Wang, M. Xu, Y. Liu, Y. Jin, W. Huang, J. Wang, *Adv. Opt. Mater.* **2019**, *7*, 1801575.
- [25] B. P. Kore, W. Zhang, B. W. Hoogendoorn, M. Safdari, J. M. Gardner, *Commun. Mater.* **2021**, *2*, 100.
- [26] Z. Wang, Q. Lin, F. P. Chmiel, N. Sakai, L. M. Herz, H. J. Snaith, *Nat. Energy* **2017**, *2*, 17135.
- [27] C. R. Kagan, D. B. Mitzi, C. D. Dimitrakopoulos, *Science* **1999**, *286*, 945.
- [28] D. B. Mitzi, C. A. Feild, W. T. A. Harrison, A. M. Guloy, *Nature* **1994**, *369*, 467.
- [29] C. G. Bischak, C. L. Hetherington, H. Wu, S. Aloni, D. F. Ogletree, D. T. Limmer, N. S. Ginsberg, *Nano Lett.* **2017**, *17*, 1028.
- [30] F. Huang, P. Siffalovic, B. Li, S. Yang, L. Zhang, P. Nadazdy, G. Cao, J. Tian, *Chem. Eng. J.* **2020**, *394*, 124959.
- [31] G. Grancini, M. K. Nazeeruddin, *Nat. Rev. Mater.* **2019**, *4*, 4.
- [32] J. Hu, I. W. H. Oswald, S. J. Stuard, M. M. Nahid, N. Zhou, O. F. Williams, Z. Guo, L. Yan, H. Hu, Z. Chen, X. Xiao, Y. Lin, Z. Yang, J. Huang, A. M. Moran, H. Ade, J. R. Neilson, W. You, *Nat. Commun.* **2019**, *10*, 1276.
- [33] M. E. Kamminga, H. H. Fang, M. R. Filip, F. Giustino, J. Baas, G. R. Blake, M. A. Loi, T. T. M. Palstra, *Chem. Mater.* **2016**, *28*, 4554.
- [34] N. R. Venkatesan, J. G. Labram, M. L. Chabiny, *ACS Energy Lett.* **2018**, *3*, 380.
- [35] S. Shao, H. Duim, Q. Wang, B. Xu, J. Dong, S. Adjokatse, G. R. Blake, L. Protesescu, G. Portale, J. Hou, M. Saba, M. A. Loi, *ACS Energy Lett.* **2020**, *5*, 39.
- [36] J. Liu, J. Leng, K. Wu, J. Zhang, S. Jin, *J. Am. Chem. Soc.* **2017**, *139*, 1432.
- [37] G. Xing, B. Wu, X. Wu, M. Li, B. Du, Q. Wei, J. Guo, E. K. L. Yeow, T. C. Sum, W. Huang, *Nat. Commun.* **2017**, *8*, 14558.
- [38] C. Li, J. Yang, F. Su, J. Tan, Y. Luo, S. Ye, *Nat. Commun.* **2020**, *11*, 5481.
- [39] X. Hong, T. Ishihara, A. U. Nurmikko, *Phys. Rev. B* **1992**, *45*, 6961.
- [40] J. D. Ziegler, J. Zipfel, B. Meisinger, M. Menahem, X. Zhu, T. Taniguchi, K. Watanabe, O. Yaffe, D. A. Egger, A. Chernikov, *Nano Lett.* **2020**, *20*, 6674.
- [41] A. Simbula, R. Pau, Q. Wang, F. Liu, V. Sarritzu, S. Lai, M. Lodde, F. Mattana, G. Mula, A. G. Lehmann, I. D. Spanopoulos, M. G. Kanatzidis, D. Marongiu, F. Quochi, M. Saba, A. Mura, G. Bongiovanni, *Adv. Opt. Mater.* **2021**, *9*, 2100295.
- [42] R. D. J. Oliver, Y.-H. Lin, A. J. Horn, C. Q. Xia, J. H. Warby, M. B. Johnston, A. J. Ramadan, H. J. Snaith, *ACS Energy Lett.* **2020**, *5*, 3336.
- [43] J. Gebhardt, Y. Kim, A. M. Rappe, *J. Phys. Chem. C* **2017**, *121*, 6569.
- [44] O. G. Reid, M. Yang, N. Kopidakis, K. Zhu, G. Rumbles, *ACS Energy Lett.* **2016**, *1*, 561.
- [45] T. A. S. Doherty, A. J. Winchester, S. Macpherson, D. N. Johnstone, V. Pareek, E. M. Tennyson, S. Kosar, F. U. Kosasih, M. Anaya, M. Abdi-Jalebi, Z. Andaji-Garmaroudi, E. L. Wong, J. Madéo, Y.-H. Chiang, J.-S. Park, Y.-K. Jung, C. E. Petoukhoff, G. Divitini, M. K. L. Man, C. Ducati, A. Walsh, P. A. Midgley, K. M. Dani, S. D. Stranks, *Nature* **2020**, *580*, 360.
- [46] S. Jariwala, H. Sun, G. W. P. Adhyaksa, A. Lof, L. A. Muscarella, B. Ehrler, E. C. Garnett, D. S. Ginger, *Joule* **2019**, *3*, 3048.
- [47] M. N. Saha, *Proc. R. Soc. London, Ser. A* **1921**, *99*, 135.
- [48] J. Fu, Q. Xu, G. Han, B. Wu, C. Hon, A. Huan, M. L. Leek, T. C. Sum, *Nat. Commun.* **2017**, *8*, 1300.
- [49] L. A. Muscarella, E. M. Hutter, J. M. Frost, G. G. Grimaldi, J. Versluis, H. J. Bakker, B. Ehrler, *J. Phys. Chem. Lett.* **2021**, *12*, 4118.
- [50] T. Ishihara, J. Takahashi, T. Goto, *Phys. Rev. B* **1990**, *42*, 11099.
- [51] R. J. Elliott, *Phys. Rev.* **1957**, *108*, 1384.
- [52] X. Xia, W. Wu, H. Li, B. Zheng, Y. Xue, J. Xu, D. Zhang, C. Gao, X. Liu, *RSC Adv.* **2016**, *6*, 14792.
- [53] C. L. Davies, J. Borchert, C. Q. Xia, R. L. Milot, H. Kraus, M. B. Johnston, L. M. Herz, *J. Phys. Chem. Lett.* **2018**, *9*, 4502.
- [54] B. Subedi, L. Guan, Y. Yu, K. Ghimire, P. Uprety, Y. Yan, N. J. Podraza, *Sol. Energy Mater. Sol. Cells* **2018**, *188*, 228.
- [55] Y. Q. Zhao, Q. R. Ma, B. Liu, Z. L. Yu, J. Yang, M. Q. Cai, *Nanoscale* **2018**, *10*, 8677.
- [56] M. Dyksik, S. Wang, W. Paritmongkol, D. K. Maude, W. A. Tisdale, M. Baranowski, P. Plochocka, *J. Phys. Chem. Lett.* **2021**, *12*, 1638.
- [57] W. Rehman, R. L. Milot, G. E. Eperon, C. Wehrenfennig, J. L. Boland, H. J. Snaith, M. B. Johnston, L. M. Herz, *Adv. Mater.* **2015**, *27*, 7938.
- [58] J. Lim, M. T. Hörantner, N. Sakai, J. M. Ball, S. Mahesh, N. K. Noel, Y. H. Lin, J. B. Patel, D. P. McMeekin, M. B. Johnston, B. Wenger, H. J. Snaith, *Energy Environ. Sci.* **2019**, *12*, 169.
- [59] C. L. Watts, L. Aspirtate, Y.-H. Lin, W. Li, R. Elzein, R. Addou, M. J. Hong, G. S. Herman, H. J. Snaith, J. G. Labram, *Commun. Phys.* **2020**, *3*, 73.
- [60] B. Zhang, L. Goldoni, C. Lambrushini, L. Moni, M. Imran, A. Pianetti, V. Pinchetti, S. Brovelli, L. De Trizio, L. Manna, *Nano Lett.* **2020**, *20*, 8847.
- [61] A. A. Burgos-Caminal, E. Socie, M. E. F. Bouduban, J.-E. Moser, *J. Phys. Chem. Lett.* **2020**, *11*, 18.
- [62] V. A. Hintermayr, L. Polavarapu, A. S. Urban, J. Feldmann, *ACS Nano* **2018**, *12*, 10151.
- [63] A. Kumar, A. Solanki, M. Manjappa, S. Ramesh, Y. K. Srivastava, P. Agarwal, T. C. Sum, R. Singh, *Sci. Adv.* **2020**, *6*, eaax8821.
- [64] N. Spitha, D. D. Kohler, M. P. Hautzinger, J. Li, S. Jin, J. C. Wright, *J. Phys. Chem. C* **2020**, *124*, 17430.
- [65] H. Tsai, W. Nie, J.-C. Blancon, C. C. Stoumpos, R. Asadpour, B. Harutyunyan, A. J. Neukirch, R. Verduzco, J. J. Crochet, S. Tretiak, L. Pedesseau, J. Even, M. A. Alam, G. Gupta, J. Lou, P. M. Ajayan, M. J. Bedzyk, M. G. Kanatzidis, A. D. Mohite, *Nature* **2016**, *536*, 312.